The Three Atmospheric Circulations over the Indian Ocean and the Maritime Continent and Their Modulation by the Passage of the MJO

Daria Kuznetsova, Thibaut Dauhut, Jean-Pierre Chaboureau

The Three Atmospheric Circulations over the Indian Ocean and the Maritime Continent and Their Modulation by the Passage of the MJO

DARIA KUZNETSOVA, THIBAUT DAUHUT, AND JEAN-PIERRE CHABOUREAU

Laboratoire d'Aérologie, Université de Toulouse, CNRS, UPS, Toulouse, France

(Manuscript received 3 July 2018, in final form 28 November 2018)

ABSTRACT

The passage of the Madden–Julian oscillation (MJO) over the Indian Ocean and the Maritime Continent is investigated during the episode of 23–30 November 2011. A Meso-NH convection-permitting simulation with a horizontal grid spacing of 4 km is examined. The simulation reproduces the MJO signal correctly, showing the eastward propagation of the primary rain activity. The atmospheric overturning is analyzed using the isentropic method, which separates the ascending air with high equivalent potential temperature from the subsiding air with low equivalent potential temperature. Three key circulations are found. The first two circulations are a tropospheric deep circulation spanning from the surface to an altitude of 14 km and an overshoot circulation within the tropical tropopause layer. As expected for circulations associated with deep convection, their intensities, as well as their diabatic tendencies, increase during the active phase of the MJO, while their entrainment rates decrease. The third circulation is characterized by a rising of air with low equivalent potential temperature in the lower free troposphere. The intensity of the circulation, as well as its depth, varies with the MJO activity. During the suppressed phase, this circulation is associated with a dry air intrusion from the subtropical region into the tropical band and shows a strong drying of the lower to middle troposphere.

1. Introduction

The Madden–Julian oscillation (MJO; Madden and Julian 1971, 1972), is a large-scale phenomenon (with a zonal extent of ~12 000–20 000 km) and the dominant component of the intraseasonal variability in the tropical atmosphere. It is represented by coupled patterns in atmospheric circulation and convection and is accompanied by a distinct signal in many other variables (Zhang 2005). The MJO consists of a zone of widespread, deep convection and enhanced precipitation totals, surrounded on the east and west by zones of relatively weak convection and less precipitation. The MJO propagates eastward around the globe with an intraseasonal period of approximately 30–90 days. Inside the MJO envelope, small-scale convective systems interact with mesoscale convective systems (MCSs) and superclusters, giving the convection a multiscale structure (Nakazawa 1988; Moncrieff et al. 2012). The convective signals of the MJO are generally most visible over the Indian and western Pacific Oceans (Zhang 2005), where the MJO propagates with an average speed of 5 m s^{-1}.

Corresponding author: Daria Kuznetsova, daria.kuznetsova.aero.obs.mip@gmail.com

An extensive observational field campaign, the Cooperative Indian Ocean Experiment on Intraseasonal Variability (CINDY)/Dynamics of the Madden–Julian Oscillation (DYNAMO) (Yoneyama et al. 2013; Zhang et al. 2013; Zhang and Yoneyama 2017), was conducted during the period of 2011–12. This campaign allowed the different processes that contribute to the evolution of the MJO to be observed. Kerns and Chen (2014) and Chen et al. (2016) noted that, during the episode of November 2011 (MJO-II), several large-scale dry air intrusions from the subtropics into the tropical Indian Ocean were observed. They proposed that these dry air intrusions contributed to the eastward propagation of the active MJO phase and the development of the suppressed phase in the following way. The convection located in the intertropical convergence zone (ITCZ) was forced toward the equator by a dry air intrusion, creating favorable conditions for the initiation of the MJO. The following dry air intrusions participated in the suppression of the convection to the west of the active MJO phase. These dry air intrusions are likely to be advected by Rossby wave gyres and are thus consistent with the response to equatorial heating as in Gill (1980).

This paper further describes the convective evolution of the atmosphere during the passage of the MJO and

DOI: 10.1175/JAS-D-18-0188.1

the development of the suppressed MJO phase. To have a multiscale description of convection, we performed a convection-permitting simulation over a vast domain consisting of the Indian Ocean and the Maritime Continent. A specific question addressed here is whether the dry intrusions have an imprint on the atmosphere overturning. Thus, the same period of 23–30 November 2011 of Chen et al. (2016) was chosen to analyze the transition from the active phase to the suppressed phase over the Indian Ocean and the arrival of the active phase over the Maritime Continent.

To study the large-scale atmospheric circulations, an isentropic analysis is applied. This method was first described by Pauluis and Mrowiec (2013) and allows cold, dry sinking air masses to be separated from warm, moist rising air masses by grouping air particles with similar thermodynamic properties. In addition, reversible motions are excluded via time averaging. This method has been successfully applied in a number of numerical studies, such as analyses of a very deep convective system that hydrates the stratosphere (Dauhut et al. 2017) and the October 2011 MJO event observed during the CINDY/DYNAMO campaign (Chen et al. 2018). In the latter study, the tropospheric overturning up to 16-km height was investigated by decomposition into multiple scales. It was found to be largest at the convective scale (less than 450 km) and to be increasing with the active phase of the MJO. In our paper, an isentropic analysis is applied to the November 2011 MJO event characterized by dry intrusions and using a convection-permitting simulation performed at higher resolution. This allows us to investigate the atmospheric overturning up to 18-km height with additional features. It is shown to consist of three components, or circulations in an isentropic diagram: a tropospheric circulation similar to the one found by Chen et al. (2018), a smaller circulation corresponding to dry air intrusions, and an overshoot circulation similar to the one obtained in the study of Dauhut et al. (2017). These circulations together with the diabatic tendencies and the entrainment rates are contrasted between the active and suppressed phases of the MJO, as well as between the Indian Ocean and the Maritime Continent.

Section 2 describes the model and the methodology. Section 3 analyzes the differences in the convective activity with the passage of the MJO. Section 4 discusses the signature of dry air intrusions during the MJO propagation as seen in the isentropic diagrams. Section 5 presents the conclusions.

2. Data and methods

a. Meso-NH high-resolution simulation

The simulation is run using the atmospheric nonhydrostatic regional model Meso-NH (Lafore et al. 1998; Lac et al. 2018), version 5-1-3, over the region of 26.7°S–26.7°N, 44.6°–155.4°E to include the Indian Ocean and the Maritime Continent (Fig. 1). This large domain is chosen in order to describe the large-scale variability induced by the passage of the MJO. For the analysis applied here, two subdomains are considered focusing on the Indian Ocean (7.5°S–7.5°N, 60°–80°E) and the Maritime Continent (7.5°S–7.5°N, 100°–120°E). The 8-day period of 23–30 November 2011 is simulated. The simulation is performed with a horizontal grid spacing of 4 km. A total of 72 vertical levels are used following the surface elevation with a grid spacing of 60 m near the surface and 600 m at the top of the model. The top of the model is set to 30 km with the upper 3 km being a sponge layer to damp any gravity waves generated by convection. Therefore, a domain of $1538 \times 3074 \times 72$ (~340 million) grid points is considered. It was possible to run this high-resolution simulation on a very large domain because of the parallel computing capability of the Meso-NH model (Pantillon et al. 2011).

The following parameterizations employed in the model: the Surface Externalisée (SURFEX) scheme for the surface fluxes (Masson et al. 2013), the microphysical scheme ICE3 (Pinty and Jabouille 1998) for the mixed-phase clouds containing five hydrometeor types (cloud water, rain, snow, graupel, and ice), a subgrid statistical cloud scheme (Chaboureau and Bechtold 2005), and a subgrid shallow convection parameterization (Pergaud et al. 2009). The radiative schemes used were the Rapid Radiative Transfer Model (Mlawer et al. 1997) for longwave radiation and the two-stream formulation (Fouquart and Bonnel 1986) for shortwave radiation. The turbulence is described using the 1.5-order closure scheme of Cuxart et al. (2000). This scheme was set in our simulation in 3D mode with the mixing length of Deardorff (1980) to obtain a better representation of the cloud organization and their lifetime duration, as shown in Machado and Chaboureau (2015).

The model is initialized at 0000 UTC 23 November 2011. The initial and boundary conditions are provided by the 6-hourly operational analyses of the European Centre for Medium-Range Weather Forecasts (ECMWF). No large-scale forcing is applied. The sea surface temperature was set using the values provided by the ECMWF analyses at the initial time. To assess the simulated rain, the TRMM 3B42 precipitation product (Huffman et al. 2007) with 3-h temporal resolution and a spatial resolution of $0.25° \times 0.25°$ is used.

b. Isentropic analysis

An isentropic analysis is applied to describe the air mass overturning at the regional scale, eliminating any reversible oscillatory motions. For details, the reader is

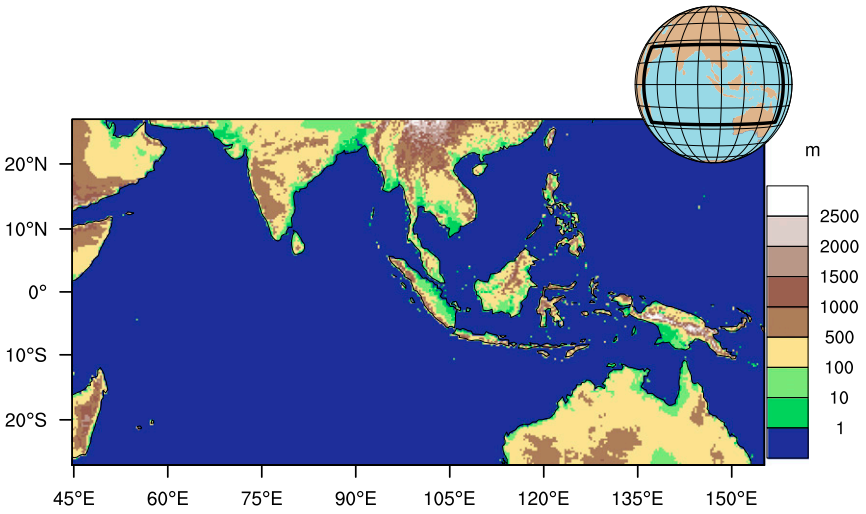

FIG. 1. Domain of simulation (Indian Ocean and Maritime Continent), with elevation (m) shaded.

referred to Pauluis and Mrowiec (2013) and Dauhut et al. (2017). In this method, the atmospheric circulations are described using a vertical coordinate and an isentropic coordinate (conserved during the reversible motions), which allows the air masses to be regrouped and reduces the four spatiotemporal coordinates to two. The dynamic and thermodynamic properties of the circulations are then investigated. As the vertical coordinate, we use the height above the ground z, while the isentropic coordinate is the equivalent potential temperature θ_e. The equivalent potential temperature was chosen as the isentropic coordinate because it is conserved in reversible moist adiabatic processes (e.g., gravity waves and transitions between water vapor and liquid water). However, during mixing, radiative processes, or phase changes involving ice, the equivalent potential temperature is no longer conserved. The equivalent potential temperature is defined by the formula of Emanuel (1994):

$$\theta_e = T\left(\frac{p_0}{p}\right)^{R_d/C_p} \exp\left(\frac{L_v r_v}{C_p T}\right) H^{-R_v r_v/C_p}. \tag{1}$$

Here T is the temperature; p_0 is the reference pressure of 1000 hPa; p is the absolute pressure; R_d and R_v are the ideal gas constants for dry air and water vapor, respectively; $C_p = C_{pd} + r_t C_l$ is the specific heat at constant pressure of moist air, where C_{pd} and C_l represent the specific heat of dry air and liquid water, respectively; r_t is the mixing ratio of vapor and liquid water; L_v is the latent heat of vaporization; r_v is the mixing ratio of the vapor; and H is the relative humidity.

The coordinate transformation is performed in the following manner:

$$\langle f\rangle(\theta_{e0}, z_0) = \frac{1}{PL_xL_y}\int_0^P\int_0^{L_y}\int_0^{L_x} f(x,y,z_0,t)\,\delta[\theta_{e0} - \theta_e(x,y,z_0,t)]\,dx\,dy\,dt, \tag{2}$$

where the units of $\langle f\rangle$ are the units of f per kelvin, and δ denotes the Dirac function, approximated numerically by $1/\Delta\theta_{e0}$ over $[\theta_{e0} - \Delta\theta_{e0}/2, \theta_{e0} + \Delta\theta_{e0}/2]$ with $\Delta\theta_{e0} = 1$ K.

An important component of the isentropic analysis is the isentropic streamfunction Ψ. It is calculated as the vertical mass flux ρw (where ρ is the density and w is the vertical velocity) from 0 to θ_{e0} at each level z_0:

$$\Psi(\theta_{e0}, z_0) = \int_0^{\theta_{e0}} \langle \rho w\rangle(\theta_e, z_0)\,d\theta_e. \tag{3}$$

This represents the net mass flux at the level z of the air parcels having an equivalent potential temperature less than or equal to θ_{e0}. From the isentropic streamfunction, it is possible to visualize the isentropic streamlines. They can be described as the averaged paths of air parcels with the same (θ_{e0}, z_0) coordinates and correspond to the Lagrangian trajectories followed by those parcels, similar to the streamlines of an unsteady flow.

3. Evolution of the convective activity during the passage of the MJO

a. MJO signal in the precipitation and an assessment of the model

To assess the quality of the simulation, a Hovmöller diagram for the precipitation averaged in the equatorial

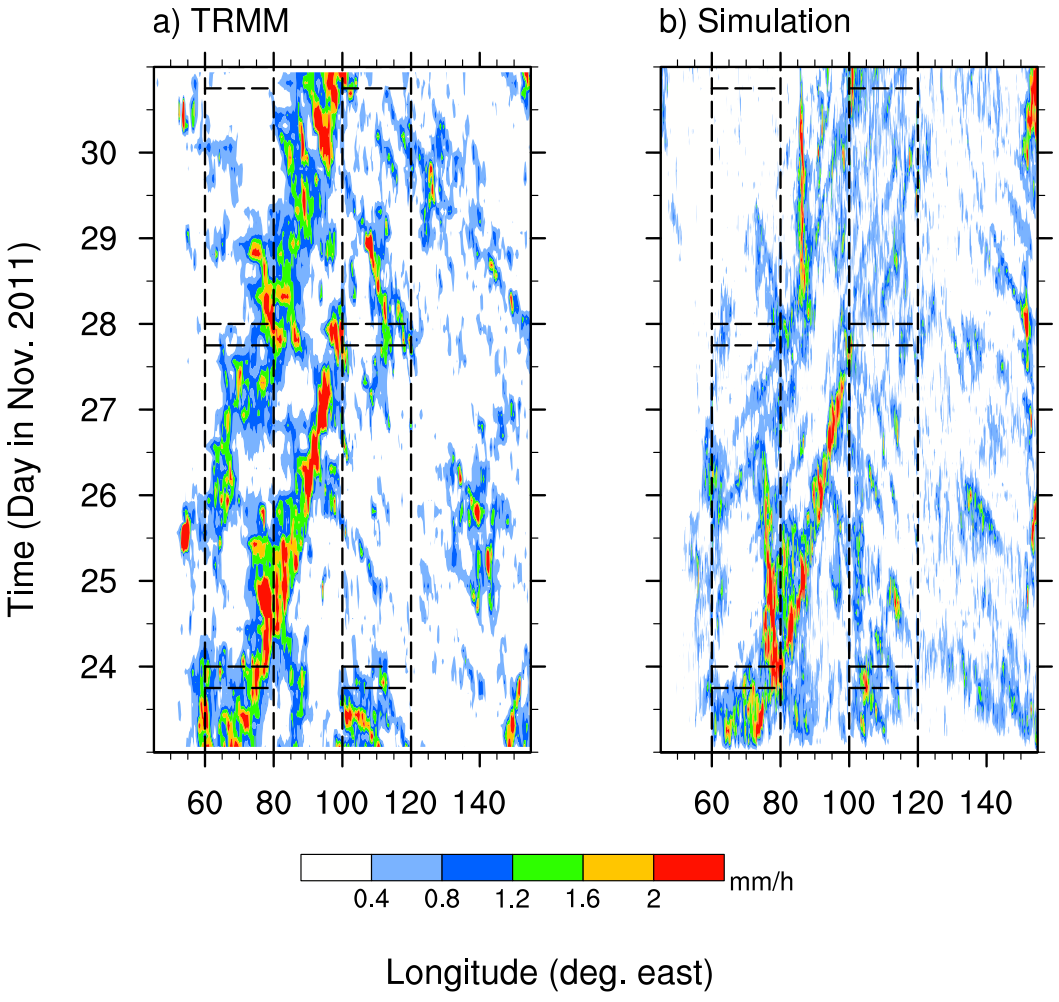

FIG. 2. Hovmöller diagram of the precipitation averaged over the region of 7.5°S–7.5°N for (a) TRMM and (b) the simulation. The vertical lines show the studied longitudinal domains: the Indian Ocean, 60°–80°E, and the Maritime Continent, 100°–120°E. The horizontal lines show the time periods chosen for the analyses of the different MJO phases.

band of 7.5°S–7.5°N is shown (Fig. 2). The longitude range corresponds to the entire simulation domain. In TRMM, the MJO signal showing the eastward propagation of the active phase over the Indian Ocean and the Maritime Continent is clearly visible (Fig. 2a). It consists of two large-scale eastward-propagating features separated by a break of 1–2 days. As noted by Kerns and Chen (2014), the dry air intrusions contribute to this break in the precipitation during the active MJO phase. The two east-propagating features look like the Kelvin waves (KWs) identified by DePasquale et al. (2014). However, their velocity, which is about 8.5 m s^{-1}, and is thus smaller than the typical values for KWs, does not allow to identify them as KWs unambiguously.

At 0000 UTC 23 November 2011, the first large-scale eastward-propagating feature characterizing the active MJO phase was located over the Indian Ocean and it arrives over the Maritime Continent around 2100 UTC 27 November 2011. The second large-scale eastward-propagating feature appears over the Indian Ocean around 1200 UTC 25 November 2011, and reaches the Maritime Continent around 1500 UTC 30 November 2011. The MJO signal is well reproduced by the simulation (Fig. 2b). The first large-scale eastward-propagating feature appears over the Indian Ocean at the same time as in TRMM and arrives over the Maritime Continent around 0000 UTC 28 November 2011. The second large-scale eastward-propagating feature appears over the Indian Ocean at the same time as in TRMM and arrives over the Maritime Continent at the end of the simulation. This feature is weaker than the first one, as well as the corresponding feature in TRMM, but is still visible. The maximum rainfall in both TRMM and the simulation exceeds 2 mm h^{-1}. Nevertheless, the

simulation gives an excess of weak precipitation, including during time periods when TRMM does not show any precipitation. This might be due to systematic errors in simulating very low rates of precipitation or because the TRMM product is not sensitive to weak precipitation.

In the following, three different periods during the MJO propagation are compared: period 1, covering 1800 UTC 23 November–0000 UTC 24 November; period 2, covering 1800 UTC 27 November–0000 UTC 28 November; and period 3, covering 1800 UTC 30 November–0000 UTC 1 December. These periods are indicated in Fig. 2 by dashed horizontal lines, while the dashed vertical lines show the longitudinal limits for the subdomains chosen for the analyses. For the Indian Ocean, period 1 corresponds to the passage of the active phase, period 2 corresponds to the transition between the active phase and the suppressed phase (hereafter the "intermediate phase"), and period 3 corresponds to the suppressed phase. For the Maritime Continent, period 1 occurs during the suppressed period between the October and November MJO events, period 2 is just before the active phase, although convection is still suppressed, and period 3 is after the beginning of the active phase.

b. *MJO propagation over the Indian Ocean and the Maritime Continent*

The probability distribution function (PDF), the isentropic vertical mass flux, and the isentropic streamfunction for the Indian Ocean (Fig. 3) and for the Maritime Continent (Fig. 4) are shown for periods 1–3. The thick black lines in the figures correspond to the average θ_e profile during the corresponding time period. This profile will be denoted hereafter as $\overline{\theta}_e$.

The PDF corresponds to the frequency of each θ_e bin at each z level and shows that the majority of the points have values of θ_e close to the average profile (Figs. 3a–c). The average profile changes with time; its minimum stays at $z \simeq 3$ km but decreases in value from $\theta_e \simeq 335$ K during the active phase (period 1), to $\theta_e \simeq 330$ K during the intermediate phase (period 2), and to $\theta_e \simeq 327$ K during the suppressed phase (period 3). As is shown in section 4, this decrease is due to the drying of the air in the lower to middle troposphere. The air parcels with larger θ_e (i.e., the parcels with θ_e exceeding the average value by several kelvins) correspond to PDF values less than 2%. Together, they account for less than 6% of the total at every z level for all three phases. In the active phase, air parcels having $\theta_e \leq 330$ K account for less than 14.6% of the total at every z level. With the decrease in $\overline{\theta}_e$ with time, the percentage of these low-θ_e points increases up to 47.9% in the intermediate phase and 63.8% in the suppressed phase. This feature is especially noticeable between $z \simeq 3$ and $z \simeq 6$ km.

The vertical mass flux consists of two main parts in the troposphere (Figs. 3d–f). The first part corresponds to upward motions with θ_e higher than $\overline{\theta}_e$, and the second part corresponds to downward motions at low θ_e (generally lower than $\overline{\theta}_e$, including a small zone with $\theta_e > \overline{\theta}_e$). Above 14–15 km, an upward motion is observed with $\theta_e < \overline{\theta}_e$ and a downward motion is seen with $\theta_e > \overline{\theta}_e$. The rising motion of air parcels with $\theta_e < \overline{\theta}_e$ is a signature of overshooting into the stratosphere (Dauhut et al. 2017). The amplitudes of the tropospheric vertical mass flux and the overshoot are larger during the active phase than during the intermediate and suppressed phases. The rising air parcels are fewer in number than the descending ones, according to Figs. 3a–c. During the active and intermediate phases, small zones with low θ_e and upward motion appear, intensifying during the suppressed phase. This intensification also corresponds to an increase in the percentage of low-θ_e air parcels for z levels between 3 and 6 km, as shown previously.

The streamfunction consists of three key circulations (Figs. 3g–i). One circulation is a large-scale tropospheric circulation spanning from the surface to an altitude of 14–15 km (negative Ψ values), where the rising air parcels have high θ_e values up to 352 K. The air masses with high θ_e are ascending, while the air masses with lower θ_e are descending. The intensity of this circulation is greatest at 4 km. The second circulation is an overshoot circulation, with positive Ψ values in the tropical tropopause layer, extending from $z \simeq 13$–14 km to above 17 km. These first two circulations have a larger amplitude and vertical extent during the active phase of the MJO. The third circulation with positive Ψ values at low θ_e appears during the active and intermediate phases and intensifies during the suppressed phase. This circulation corresponds to the small zone with an upward motion (Figs. 3d–f) described previously and extends from $z \simeq 600$ m to $z \simeq 7$ km during the suppressed phase. It will be shown later that this circulation corresponds to dry air advected from the subtropics.

For the Maritime Continent, the PDF points are concentrated along the average profile (Figs. 4a–c), as in the case of the Indian Ocean. Below a height of 9 km, most of the air parcels (with a probability of more than 5%) have $|\theta_e - \overline{\theta}_e| < 10$ K, while at greater heights most of the air parcels have $|\theta_e - \overline{\theta}_e| < 5$ K. Large-θ_e air parcels (i.e., the parcels with θ_e exceeding the average value by several kelvins) correspond to PDF values of less than 2% at every point and together account for less than 3.4% at every z level during the entire simulation period. Before the arrival of the suppressed phase (during period 1) there are no points with $\theta_e < 325$ K. During the suppressed phase (period 2), the lowest θ_e value is 320 K and this value decreases further to

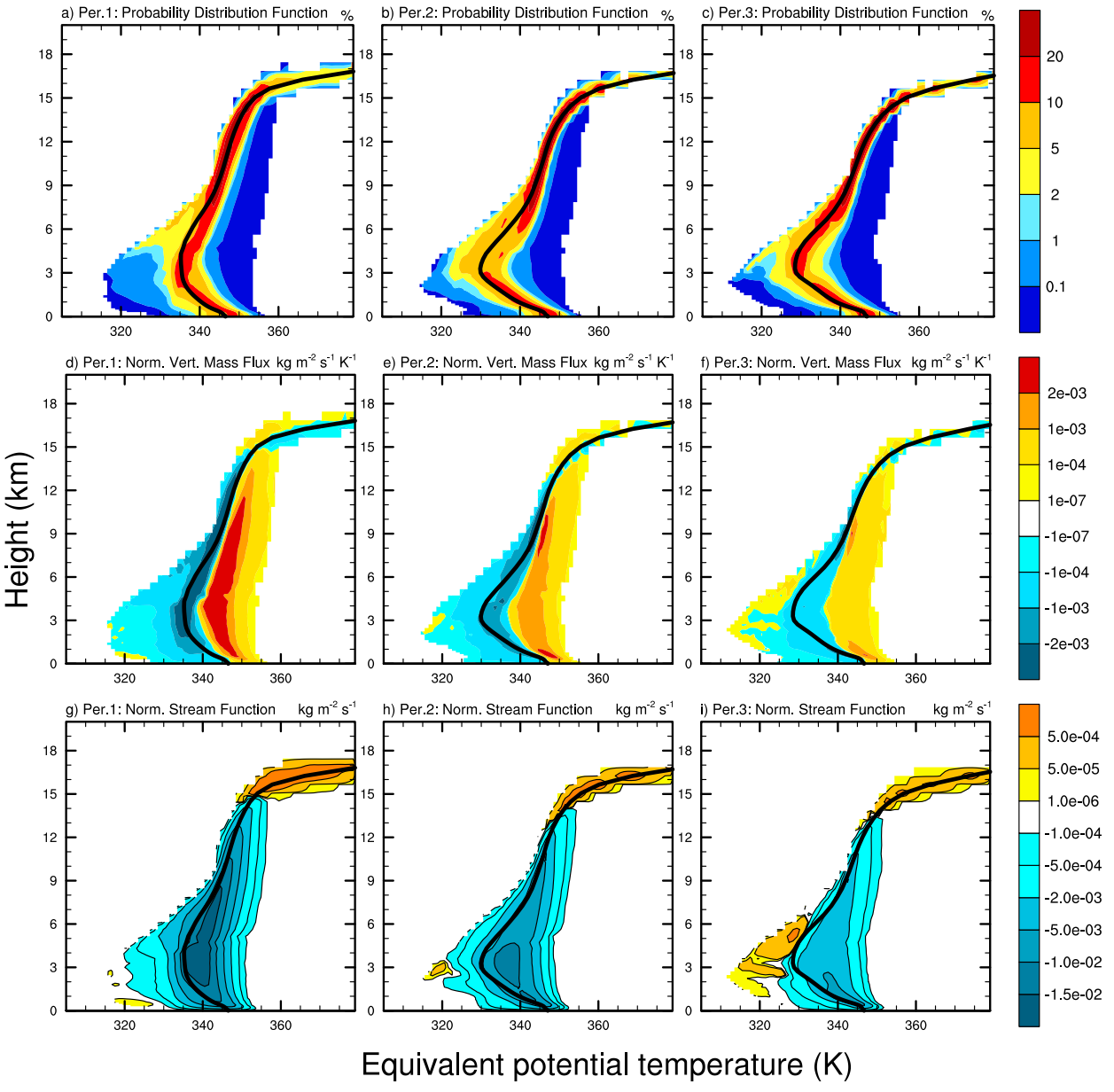

FIG. 3. Isentropic diagrams for the Indian Ocean: (a)–(c) PDF, (d)–(f) vertical mass flux, and (g)–(i) streamfunction. Columns represent (left) period 1 (the passage of the active phase), (center) period 2 (the intermediate phase between the active and the suppressed ones), and (right) period 3 (the suppressed phase). The thick black line in each panel corresponds to the θ_e profile averaged over all the grid points during the corresponding time period.

approximately 317 K at the time of the arrival of the active phase (period 3). During the suppressed phase and just before the arrival of the active phase (period 2), the percentage of air parcels with low θ_e (<327 K) does not exceed 4.5% at any z level. During the active phase, the frequency of air masses with $\theta_e < \overline{\theta}_e$ increases. The average profile of θ_e does not change with the passage of the MJO, unlike in the case of the Indian Ocean.

The vertical mass flux (Figs. 4d–f) for $z < 13$–14 km consists of a zone with higher θ_e characterized by rising air and a zone with lower θ_e corresponding to descending air. The descending air parcels are located close to the average profile and, as shown previously, represent a higher percentage than that of the rising air parcels. For $z > 14$ km, the air with $\theta_e < \overline{\theta}_e$ is rising while the air with larger θ_e is descending. This corresponds to an overshoot circulation, as in the case of the Indian Ocean.

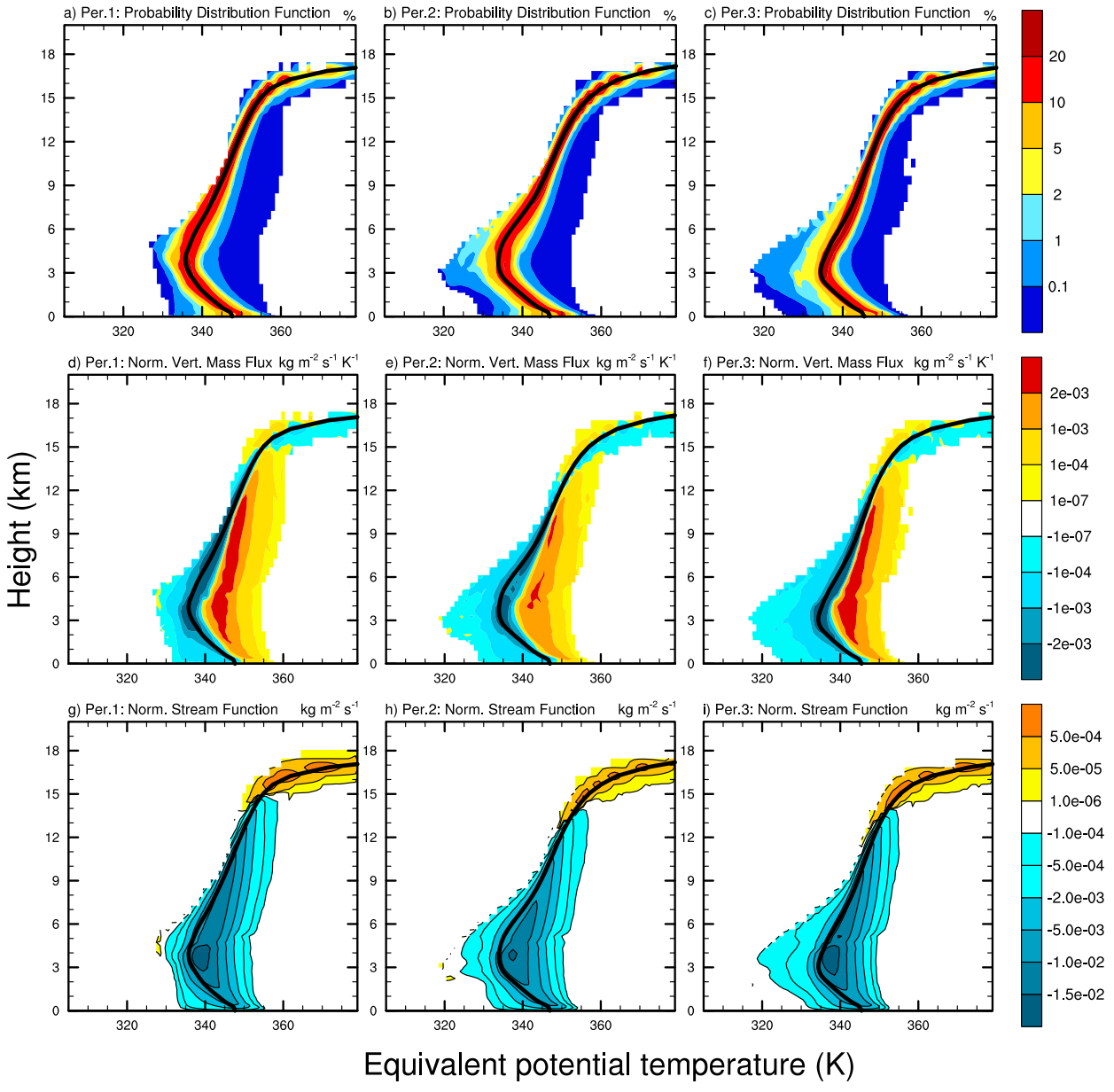

FIG. 4. As in Fig. 3, but for the Maritime Continent. (left) Period 1 occurs during the suppressed MJO phase, (center) period 2 is just before the active phase, although convection is still suppressed, and (right) period 3 is after the beginning of the active phase.

There are a few low-θ_e zones with rising motion on average near $z \simeq 2$–5 km during periods 1 and 2. However, their intensity is weak and their corresponding percentage is less than 1%. An intensification in the large-scale rising and descending motions is visible during the active MJO phase, and the weakest amplitude corresponds to the suppressed MJO phase.

In all the phases, the streamfunction (Figs. 4g–i) consists of a large-scale tropospheric circulation and an overshoot circulation. The third circulation, similar to that identified over the Indian Ocean, appears prior to the passage of the suppressed phase of the MJO and remains during the suppressed phase but with much weaker intensity. Unlike the streamfunction for the Indian Ocean (Figs. 3g–i), the intensities of the large-scale circulation and the overshoot circulation do not change significantly over the Maritime Continent during the passage of the MJO.

c. *Diabatic tendencies and entrainment*

To further continue this analysis and to better understand the large-scale thermodynamical properties of

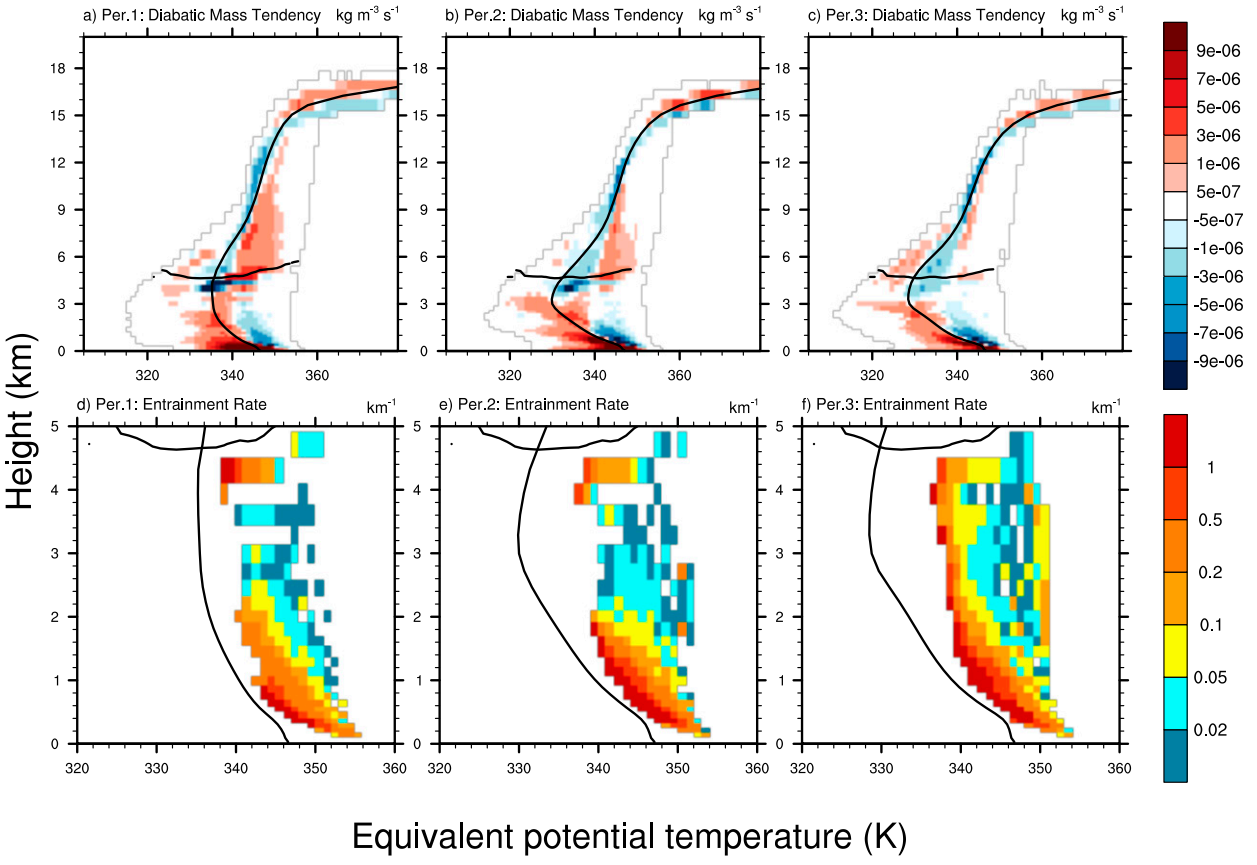

FIG. 5. Isentropic diagrams for the Indian Ocean: (a)–(c) diabatic tendency and (d)–(f) entrainment rate. Columns represent (left) period 1, (center) period 2, and (right) period 3. The black line near $z = 5$ km corresponds to the average freezing level. The gray contour shows the isentropic envelope. The average θ_e profile is also shown.

the system, the diabatic tendency is calculated. The mass-weighted diabatic tendency $\langle \rho \dot{\theta}_e \rangle$ can be calculated as the vertical derivative of the streamfunction in a domain with periodic boundary conditions for an atmosphere in statistical radiative–convective equilibrium (Pauluis and Mrowiec 2013). Its computation can be further generalized for any boundary conditions and time evolution as described by Dauhut et al. (2017), allowing the diabatic tendency to be calculated in our study.

For the Indian Ocean, the diabatic tendencies for the three phases are shown in Figs. 5a–c, respectively. Below a height of 3 km, the diabatic tendencies have a dipole structure for all three phases. The most significant diabatic process leading to the changes in θ_e in the lower troposphere is mixing and radiation. The latter acts to cool clear-sky areas (i.e., those with low θ_e) while having negligible impact in convective areas (Dauhut et al. 2017). The air parcels with high θ_e (exceeding 342 K) have a negative diabatic tendency. These are rising air masses that are cooling and drying via mixing with the surrounding air. The air parcels with lower θ_e have a positive diabatic tendency showing warming and moistening behavior. Just below the freezing level, the diabatic tendency is negative, with a pronounced minimum in the active and intermediate phases. This likely corresponds to latent heat absorption due to ice melting and radiative cooling. Between the freezing level and $z \simeq 14$ km, the diabatic tendencies also show a dipole structure; however, air parcels with high θ_e have a positive diabatic tendency, while air parcels with low θ_e have a negative diabatic tendency. We suggest interpreting the diabatic tendencies as follows. The high-θ_e air parcels undergo latent heat release due to ice formation, which contributes to the positive diabatic tendency, exceeding the negative diabatic tendency due to mixing. The lower-θ_e air parcels have a negative diabatic tendency due to mixing with the lower-environmental-θ_e air masses, as well as due to ice sublimation and radiative cooling. In periods 1 and 3 (Figs. 5a,c), a small number of air parcels with $\theta_e < 334$ K located above the freezing level have positive diabatic tendencies probably due to

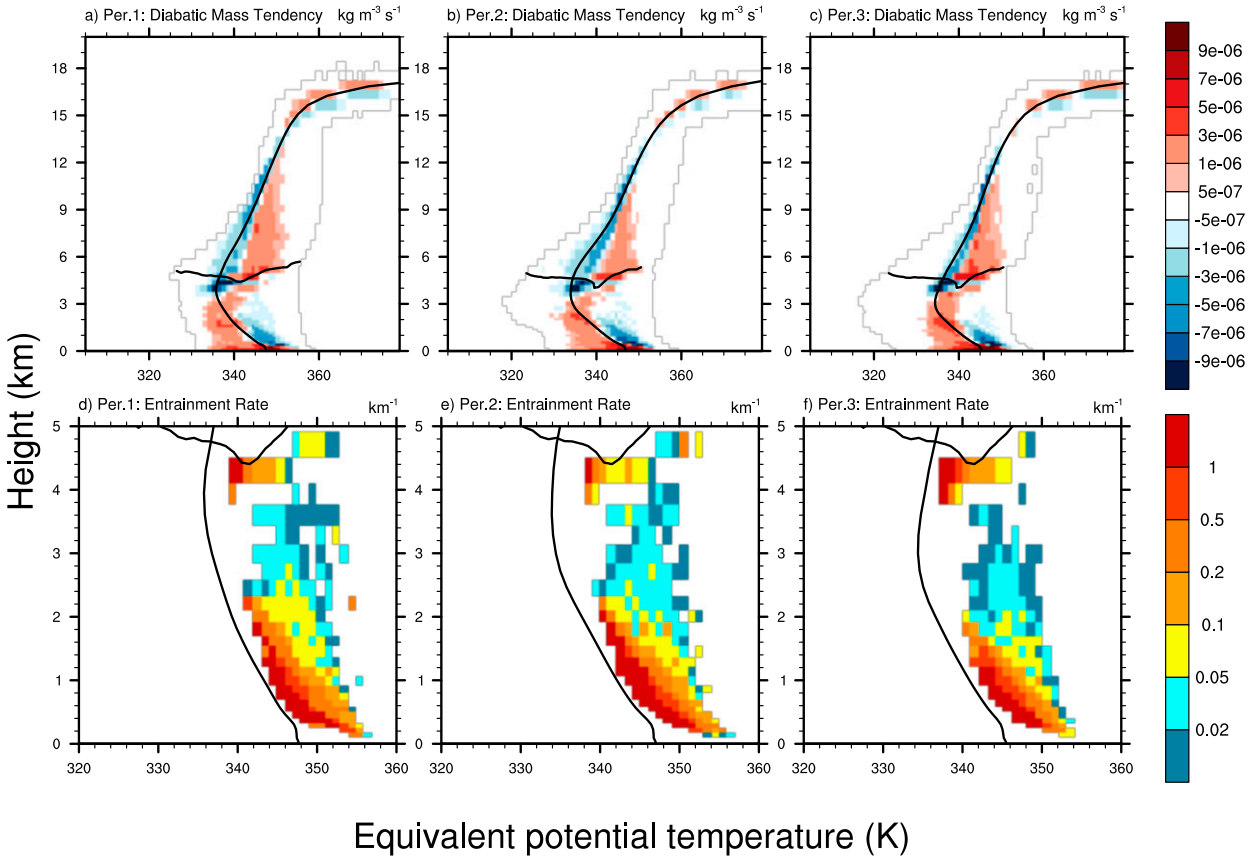

FIG. 6. As in Fig. 5, but for the Maritime Continent.

mixing because most of the air parcels have larger θ_e. In the overshoot circulation (Figs. 5a–c), the air masses with $\theta_e > \overline{\theta}_e$ have a negative diabatic tendency while those with $\theta_e < \overline{\theta}_e$ have a positive diabatic tendency. These tendencies are mostly due to mixing, similar to the air masses in the lower troposphere, but the contribution of the radiation might also exist (Dauhut et al. 2017). The amplitude of the diabatic tendencies is the largest in the active phase (period 1) and the smallest in the suppressed phase (period 3). This is in agreement with the strong convective activity during the active MJO phase and its weakening during the suppressed MJO phase.

For the Maritime Continent (Figs. 6a–c), the diabatic tendencies have a similar structure to those for the Indian Ocean (Figs. 5a–c). Nevertheless, the diabatic tendencies in the overshoot circulation have smaller values. Another difference is the absence of low-θ_e air parcels with positive diabatic tendencies close to the freezing level.

The rising air parcels entrain the environmental air. The entrainment rate ε is computed in the form of an isentropic analysis using

$$\varepsilon(\theta_e^{\text{env}} - \theta_e) = \frac{\langle \rho \dot{\theta}_e \rangle}{\langle \rho w \rangle}, \tag{4}$$

where θ_e^{env} indicates the environmental profile of θ_e. The entrainment rate is calculated here in a manner similar to that of Dauhut et al. (2017), while the average profile is used as the environmental profile. This is a reasonable assumption as the average profile is close to the PDF maxima at every height (Figs. 3a–c and 4a–c). One condition to compute ε from Eq. (4) is that θ_e variations are solely due to mixing. This is the case below 4 km. Above, the ice processes and radiation produce diabatic tendencies that prevent the use of Eq. (4) (Dauhut et al. 2017). Therefore, only the entrainment below the freezing level is considered.

The entrainment rate for the Indian Ocean is shown in Figs. 5d–f. The air masses with θ_e close to $\overline{\theta}_e$ have an entrainment rate larger than 1 km^{-1}, while the points with the largest θ_e values have a weaker entrainment rate of less than 0.05 km^{-1}. As the largest-θ_e air masses are located in the core of wide updrafts, they are likely less affected by the entrainment and the subsequent mixing with environmental air. A similar spectrum of entrainment rates as a function of the airmass θ_e was found for

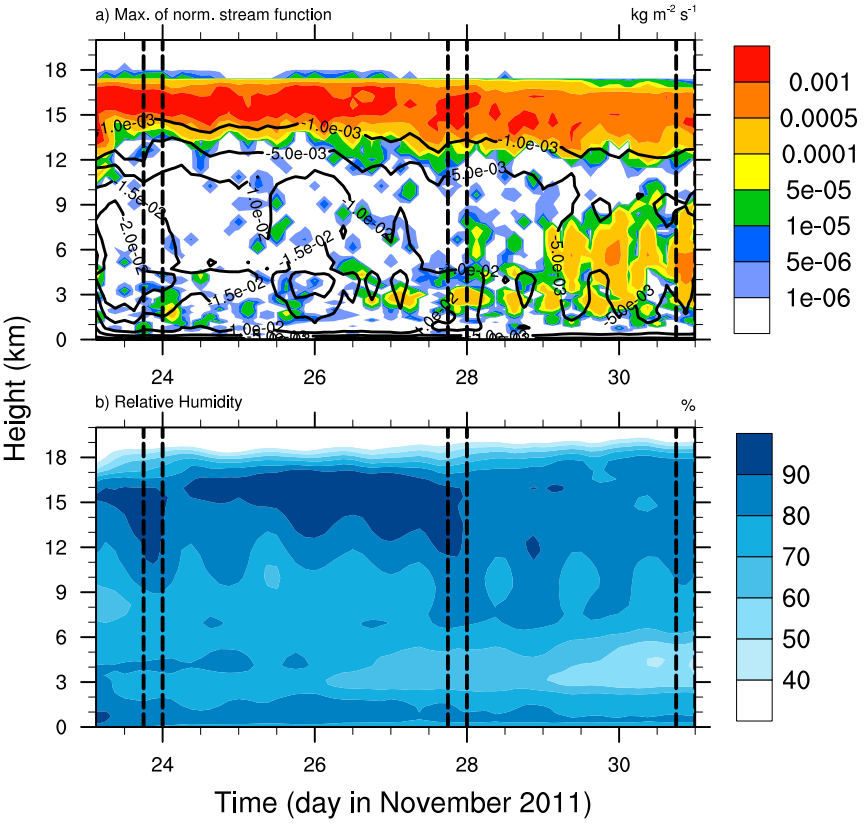

FIG. 7. Evolution of (a) the isentropic streamfunction maximum and (b) the relative humidity for the Indian Ocean. The black contours in (a) correspond to the evolution of isentropic streamfunction minimum. The vertical lines show the time periods (periods 1–3) chosen for the analyses of the different MJO phases.

the tropical multicellular storm studied by Dauhut et al. (2017), suggesting the importance of a varying entrainment rate in convection parameterization (Del Genio et al. 2012). Note that the entrainment increases during the suppressed phase (period 3). This could be explained by the change of environment in which the updrafts develop. The dry air intrusions (discussed in the following) lead the rising air masses to experience a stronger θ_e decrease when mixed with the environment, leading to larger entrainment values during the suppressed phase. The entrainment rates over the Maritime Continent (Figs. 6d–f) are similar to those over the Indian Ocean in the amplitude, the largest entrainment rate being close to the average θ_e profile. The entrainment rate decreases in period 1. This corresponds to the result obtained for the Indian Ocean (i.e., the largest entrainment rate corresponds to the suppressed phase of the MJO).

d. *Changes in the intensity of the overturning circulations*

To better understand the evolution of the large-scale circulations, it is also possible to consider the evolution of a streamfunction calculated in the same way as the isentropic streamfunction in Eq. (3) but without time averaging the vertical mass flux. Using this method, a streamfunction at every output time is obtained.

For the Indian Ocean, the time evolutions of the maximum and minimum of this streamfunction, together with the time evolution of the average relative humidity, are shown in Figs. 7a and 7b. The overshoot circulation is visible with the highest values of the maximum of the streamfunction located at z between 14 and 17 km. The intensity of the overshoot is highest at the beginning of the simulation and gradually decreases with time. The low-θ_e circulation in the streamfunction can also be traced using the streamfunction maximum, but in the low troposphere. At the beginning of the simulation, this circulation is weak with a local maximum exceeding 0.0001 kg m^{-2} s^{-1} at 0000 UTC 24 November near $z = 2$ km. This circulation then starts developing vertically after 0000 UTC 28 November and reaches 10 km around 1200 UTC 30 November. At several times (around 0000 and 2100 UTC 30 November) the associated values exceed

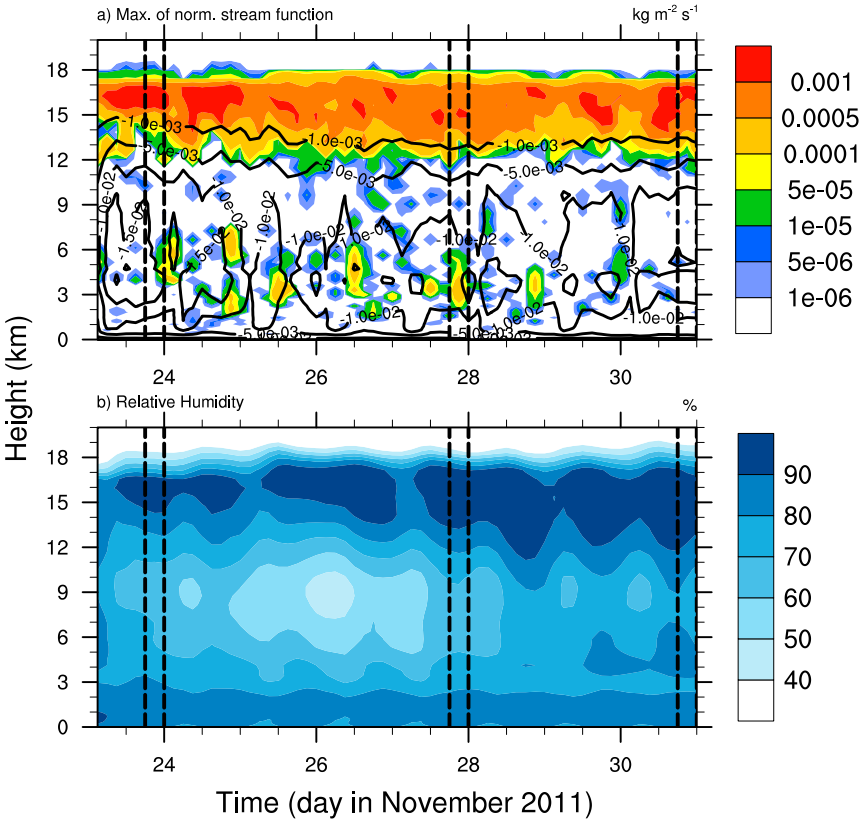

FIG. 8. As in Fig. 7, but for the Maritime Continent.

0.0005 kg m^{-2} s^{-1}. A short time-scale variability is also observed, corresponding approximately to the diurnal variability. The tropospheric circulation is depicted by the minimum of the streamfunction. It is the most developed during the active phase of the MJO as stated previously. A second maximum is also present near 0000 UTC 26 November, and a third maximum is present near 1500 UTC 28 November both located near 4 km. A moistening of the upper troposphere is visible during the active and intermediate phases of the MJO (23–28 November), as shown in Fig. 7b, while during the suppressed phase (29 November–1 December), a drying of the lower troposphere is observed. This drying extends in depth with time. At 0000 UTC 1 December, the relative humidity is less than 60% at z between 3 and 5 km, and less than 80% at z between 0.5 and 3 km. A similar drying was described by Wang et al. (2015) as observed in the North Sounding Array during the CINDY/DYNAMO campaign. Hagos et al. (2014) showed the drying during the transition from the active phase of the MJO to the suppressed phase during 3–4 days.

For the Maritime Continent, the overshoot circulation has its largest intensity at the beginning and end of the simulation (Fig. 8a). The low-θ_e circulation is not very well developed, with discrete maxima between 0.0001 and 0.0005 kg m^{-2} s^{-1} for z between 2 and 7 km, until 0000 UTC 29 November. The upper troposphere shows a diurnal variability in its relative humidity (Fig. 8b) and is the closest to saturation at the end of the simulation. The strong drying of the middle troposphere is visible from 0000 UTC 25 November to 1200 UTC 27 November, corresponding to the largest amplitudes of the low-θ_e circulation in Fig. 8a. In contrast with the Indian Ocean, the drying does not extend down to the lower troposphere. The relative humidity decreases below 60% at z between 6 and 12 km while remaining above 80% at z between 0 and 2.5 km all along the simulation.

4. Signature of dry air intrusions in the propagation of the MJO

As discussed in section 3b, a low-θ_e upward circulation is observed in the streamfunction plots, which is more distinct for the case of the Indian Ocean during the suppressed phase. Here, we concentrate on 1800 UTC 30 November when the suppressed MJO phase is over

the Indian Ocean. The timing corresponds with the penetration of dry air intrusions into the equatorial region of the Indian Ocean observed by Kerns and Chen (2014).

The horizontal cross sections at an altitude near 5 km (Fig. 9) allow for a better understanding of the presence of the low-θ_e circulation. The flow of air masses with low θ_e (<332 K) is transported into the Indian Ocean subdomain from the north (Fig. 9a) forming the so-called dry air intrusion. This intrusion also influences the average θ_e profile: as shown previously, the minimum of $\overline{\theta}_e$ decreased during the suppressed MJO phase over the Indian Ocean, while the changes in $\overline{\theta}_e$ over the Maritime Continent were weak. In Fig. 9b, the vertical velocity of the low-θ_e air masses (<330 K, similar to the low-θ_e circulation in Fig. 3i) is shown to isolate the dry airflow, with the zoom shown in Fig. 9c for all air masses. The vertical velocity is weak, with upward motions of up to 0.2 m s^{-1}.

The vertical section from an altitude of 0 to 7 km, corresponding to the thick black line in the horizontal cross sections (Figs. 9b,c), is shown in Fig. 10. The low-θ_e pocket is visible in Fig. 10a between $z \simeq 2$ and $z \simeq 6$ km. The corresponding vertical velocities in Fig. 10b (shown here for all θ_e) likely indicate the presence of gravity waves that could mix low-θ_e air masses with adjacent air masses when breaking. This is consistent with the gravity waves found in the lower troposphere, associated with clear variations in moisture and a stronger activity in the suppressed phase (Bellenger et al. 2017). As seen in Fig. 10c, θ_e shows a strong dependence on the relative humidity. The low-θ_e air masses have a relative humidity of less than 60%, including multiple regions where θ_e is less than 327 K and the corresponding relative humidity is less than 20%. Figure 10d shows the dry zones around a height of 5–6 km, with the lowest water vapor mixing ratio being less than 2 g kg^{-1}, which corresponds to $\theta_e < 327$ K. The shallow cloud tops are located below 3 km, suggesting that the dry air intrusion limits their vertical development. This is in agreement with the streamfunction that indicates a predominance of shallow convection during the suppressed phase (Fig. 3i) whereas deep and congestus convection dominate during the active and the intermediate phase, respectively (streamlines at largest values in Figs. 3g,h). This is also consistent with the largest values of entrainment found during the suppressed phase over the Indian Ocean.

5. Conclusions

A convection-permitting simulation of an MJO episode on 23–30 November 2011 was run to describe the evolution of the atmosphere during the passage of the MJO over the Indian Ocean and the Maritime Continent. An isentropic analysis was performed for two subdomains focusing on the central Indian Ocean and the western part of the Maritime Continent.

The isentropic analysis showed the existence of three large-scale convective circulations. The first one is a tropospheric circulation extending from the surface up to 14 km above the ground level. Its intensity increases during the active phase of the MJO and decreases during the suppressed phase, a feature also found for the October 2011 event by Chen et al. (2018).

The second circulation is an overshoot within the tropical tropopause layer, which is a new aspect in this study. Such circulation has been found for a tropical multicellular storm, but during its very deep convection phase only (Dauhut et al. 2017), and was not obtained by Chen et al. (2018). In this work, the overshoot circulation exists all along the convection-permitting simulation, over both the Indian Ocean and the Maritime Continent. Its intensity is higher during the active phase of the MJO, similar to the evolution of the tropospheric circulation. This suggests that the convective activity can impact the composition of the tropical tropopause layer significantly. Entrainment rates with values as low as 0.05 km^{-1} are seen for the air masses with the largest θ_e values. Similar low values were found for the very deep convective system analyzed by Dauhut et al. (2017) and partly explain the existence of the overshoot circulation. Understanding the reasons for the continuous presence of the overshoot circulation as well as its significance for water vapor transport into the stratosphere will be subject of future research.

The third circulation is characterized by low θ_e values and is located in the lower free troposphere, more pronounced in the case of the Indian Ocean. Unlike the two other circulations, the low-θ_e circulation intensifies and becomes much stronger during the suppressed phase of the MJO. The appearing of this circulation and its evolution with the MJO passage is another new finding of this study. The development of the low-θ_e circulation is related to the dry air intrusions from the subtropical zones into the equatorial region, which contributes to a further suppression of the convection after the passage of the active MJO phase. While the dry air intrusions have already been observed during the November 2011 episode of the MJO (Kerns and Chen 2014), we show that they can be identified by means of the isentropic analysis. The mean vertical motion observed during CINDY/DYNAMO (e.g., Johnson and Ciesielski 2013) is further investigated here by decomposition according to θ_e values. This allows us to reveal the vertical motions associated with the dry air intrusions. Low-θ_e air masses might be

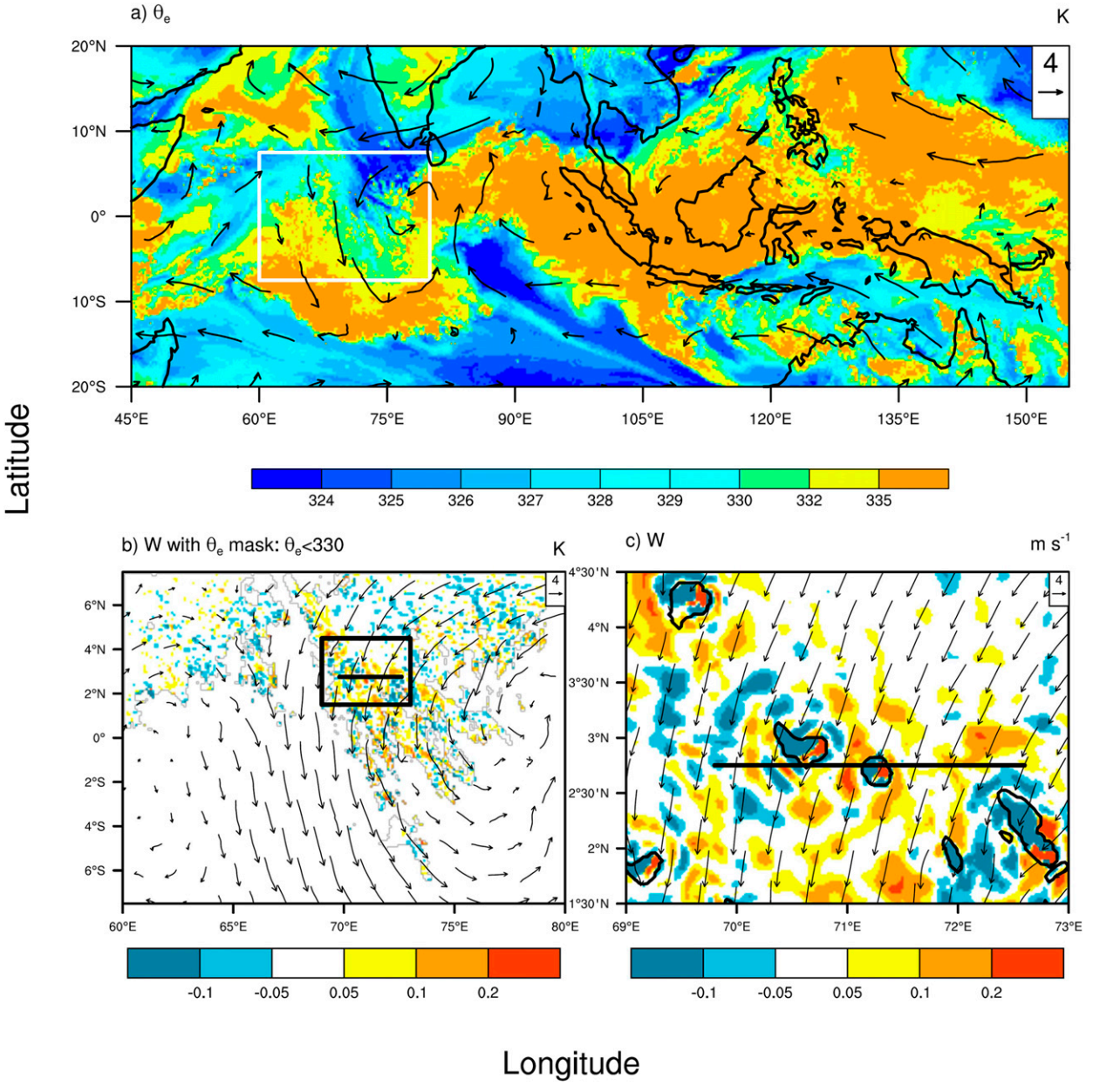

FIG. 9. (a) Spatial distribution of θ_e at 4.9-km height at 1800 UTC 30 Nov for the entire simulation domain. The white rectangle denotes the Indian Ocean subdomain (7.5°S–7.5°N, 60°–80°E). (b) Horizontal section of the vertical velocity for $\theta_e < 330$ K for the domain shown by the white rectangle in (a). The black rectangle denotes the zoom on 1.5°–4.5°N, 69°–73°E. (c) Horizontal section of the vertical velocity (for all θ_e) for the domain shown by the black rectangle in (b). The black contour shows the cloud envelope at 0.001 g kg^{-1}. The arrows in all panels represent the horizontal wind at 4.9-km height. The black line in (b) and (c) corresponds to the vertical sections shown in Fig. 10.

transported up by gravity waves. Investigations of additional MJO episodes are necessary in order to understand whether dry air intrusions are common in the passage of the MJO and to assess their inhibiting role in the development of convection.

The diabatic tendencies do not show any significant changes in structure during the passage of the MJO. Their amplitudes, however, change with the convective activity, with increases in the amplitudes occurring during the active phase. Such increases are more pronounced over the Indian Ocean than over the Maritime Continent. The entrainment rates increase during the suppressed phase of the MJO over the Indian Ocean, and in a lesser extent over the Maritime Continent. These variations are attributed to the dry air intrusions that lead the mixing between the rising motions and their environment to

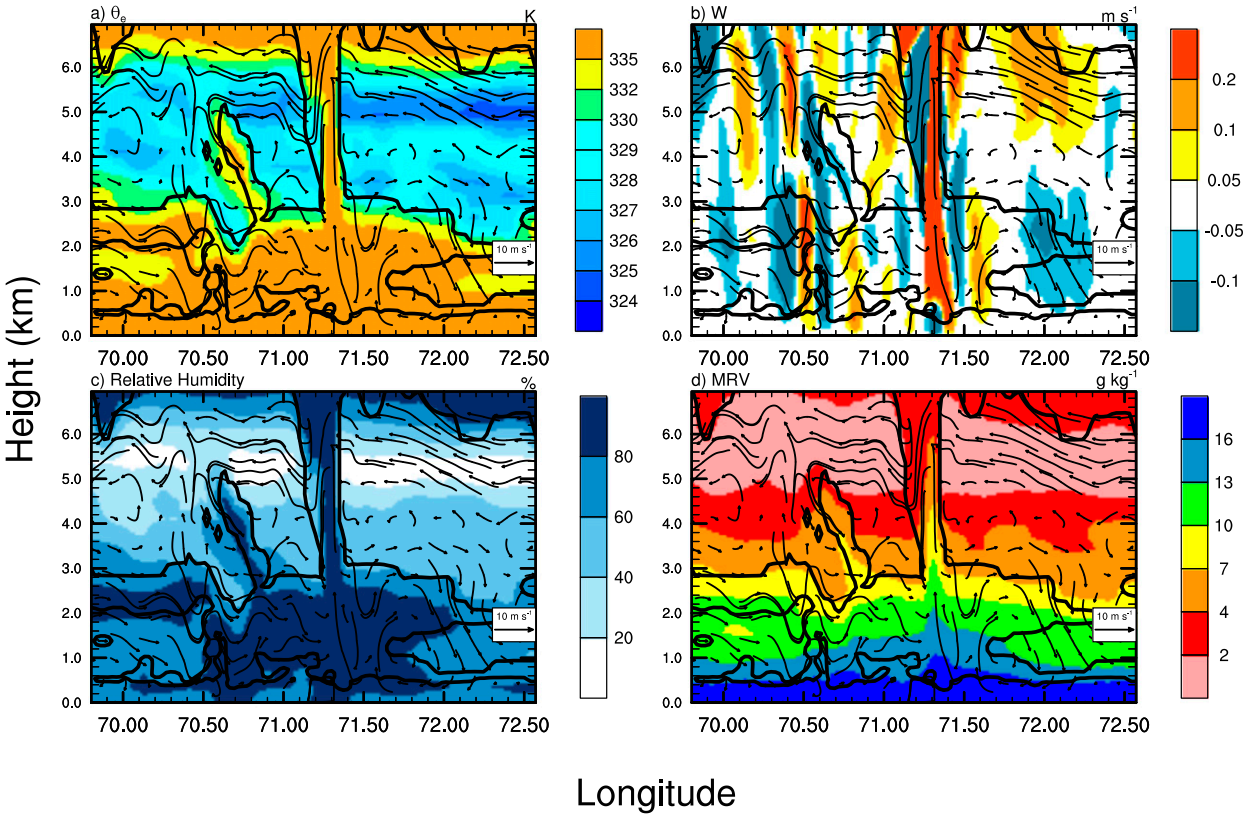

FIG. 10. Vertical section of (a) θ_e, (b) vertical velocity, (c) relative humidity, and (d) water vapor mixing ratio at 1800 UTC 30 Nov along 2.75°N latitude. The height range is 0–7 km, and the longitude range is 69.8°–72.6°E. The black contour shows the cloud envelope at 0.001 g kg^{-1}. The arrows represent the tangent wind (the vertical component has been multiplied by a factor of 100).

have a stronger inhibiting impact on convection. Further research on dry air intrusions may help in understanding their role in inhibiting convection and drying the lower troposphere and whether this gradual drying is due to gravity wave breaking. Finally, the findings here are based on a simulation that mimics well the passage of the MJO over the Indian Ocean, but that prevents precipitation from crossing the Maritime Continent. As a result, changes of smallest amplitude in different characteristics of the atmospheric overturning over the Maritime Continent should be taken with caution.

Acknowledgments. Computer resources were allocated by GENCI through Project 90569. Thibaut Dauhut is supported by the IDEX TEASAO project. We thank the anonymous reviewers for their comments, which helped to improve the overall quality of the paper.

REFERENCES

Bellenger, H., R. Wilson, J. L. Davison, J. P. Duvel, W. Xu, F. Lott, and M. Katsumata, 2017: Tropospheric turbulence over the tropical open ocean: Role of gravity waves. *J. Atmos. Sci.*, **74**, 1249–1271, https://doi.org/10.1175/JAS-D-16-0135.1.

Chaboureau, J.-P., and P. Bechtold, 2005: Statistical representation of clouds in a regional model and the impact on the diurnal cycle of convection during Tropical Convection, Cirrus and Nitrogen Oxides (TROCCINOX). *J. Geophys. Res.*, **110**, D17103, https://doi.org/10.1029/2004JD005645.

Chen, S. S., and Coauthors, 2016: Aircraft observations of dry air, the ITCZ, convective cloud systems, and cold pools in MJO during DYNAMO. *Bull. Amer. Meteor. Soc.*, **97**, 405–423, https://doi.org/10.1175/BAMS-D-13-00196.1.

Chen, X., O. M. Pauluis, and F. Zhang, 2018: Atmospheric overturning across multiple scales of an MJO event during the CINDY/DYNAMO campaign. *J. Atmos. Sci.*, **75**, 381–399, https://doi.org/10.1175/JAS-D-17-0060.1.

Cuxart, J., P. Bougeault, and J.-L. Redelsperger, 2000: A turbulence scheme allowing for mesoscale and large-eddy simulations. *Quart. J. Roy. Meteor. Soc.*, **126**, 1–30, https://doi.org/10.1002/qj.49712656202.

Dauhut, T., J.-P. Chaboureau, P. Mascart, and O. Pauluis, 2017: The atmospheric overturning induced by Hector the Convector. *J. Atmos. Sci.*, **74**, 3271–3284, https://doi.org/10.1175/JAS-D-17-0035.1.

Deardorff, J. W., 1980: Stratocumulus-capped mixed layers derived from a three-dimensional model. *Bound.-Layer Meteor.*, **18**, 495–527, https://doi.org/10.1007/BF00119502.

Del Genio, A. D., Y. Chen, D. Kim, and M. Yao, 2012: The MJO transition from shallow to deep convection in *CloudSat*/CALIPSO data and GISS GCM simulations. *J. Climate*, **25**, 3755–3770, https://doi.org/10.1175/JCLI-D-11-00384.1.

DePasquale, A., C. Schumacher, and A. Rapp, 2014: Radar observations of MJO and Kelvin wave interactions during DYNAMO/CINDY2011/AMIE. *J. Geophys. Res. Atmos.*, **119**, 6347–6367, https://doi.org/10.1002/2013JD021031.

Emanuel, K. A., 1994: *Atmospheric Convection*. Oxford University Press, 580 pp.

Fouquart, Y., and B. Bonnel, 1986: Computations of solar heating of the Earth's atmosphere: A new parametrization. *Beitr. Phys. Atmos.*, **53**, 35–62.

Gill, A. E., 1980: Some simple solutions for heat-induced tropical circulation. *Quart. J. Roy. Meteor. Soc.*, **106**, 447–462, https://doi.org/10.1002/qj.49710644905.

Hagos, S., Z. Feng, K. Landu, and C. N. Long, 2014: Advection, moistening, and shallow-to-deep convection transitions during the initiation and propagation of Madden–Julian Oscillation. *J. Adv. Model. Earth Syst.*, **6**, 938–949, https://doi.org/10.1002/2014MS000335.

Huffman, G. J., and Coauthors, 2007: The TRMM Multisatellite Precipitation Analysis (TMPA): Quasi-global, multiyear, combined-sensor precipitation estimates at fine scales. *J. Hydrometeor.*, **8**, 38–55, https://doi.org/10.1175/JHM560.1.

Johnson, R. H., and P. E. Ciesielski, 2013: Structure and properties of Madden–Julian oscillations deduced from DYNAMO sounding arrays. *J. Atmos. Sci.*, **70**, 3157–3179, https://doi.org/10.1175/JAS-D-13-065.1.

Kerns, B., and S. Chen, 2014: Equatorial dry air intrusion and related synoptic variability in MJO initiation during DYNAMO. *Mon. Wea. Rev.*, **142**, 1326–1343, https://doi.org/10.1175/MWR-D-13-00159.1.

Lac, C., and Coauthors, 2018: Overview of the Meso-NH model version 5.4 and its applications. *Geosci. Model Dev.*, **11**, 1929–1969, https://doi.org/10.5194/gmd-11-1929-2018.

Lafore, J.-P., and Coauthors, 1998: The Meso-NH atmospheric simulation system. Part I: Adiabatic formulation and control simulations. *Ann. Geophys.*, **16**, 90–109, https://doi.org/10.1007/s00585-997-0090-6.

Machado, L. A. T., and J.-P. Chaboureau, 2015: Effect of turbulence parameterization on assessment of cloud organization. *Mon. Wea. Rev.*, **143**, 3246–3262, https://doi.org/10.1175/MWR-D-14-00393.1.

Madden, R., and P. Julian, 1971: Detection of a 40–50 day oscillation in the zonal wind in the tropical Pacific. *J. Atmos. Sci.*, **28**, 702–708, https://doi.org/10.1175/1520-0469(1971)028<0702:DOADOI>2.0.CO;2.

——, and ——, 1972: Description of global-scale circulation cells in the tropics with a 40–50 day period. *J. Atmos. Sci.*, **29**, 1109–1123, https://doi.org/10.1175/1520-0469(1972)029<1109:DOGSCC>2.0.CO;2.

Masson, V., and Coauthors, 2013: The SURFEXv7.2 land and ocean surface platform for coupled or offline simulation of Earth surface variables and fluxes. *Geosci. Model Dev.*, **6**, 929–960, https://doi.org/10.5194/gmd-6-929-2013.

Mlawer, E. J., S. J. Taubman, P. D. Brown, M. J. Iacono, and S. A. Clough, 1997: Radiative transfer for inhomogeneous atmospheres: RRTM, a validated correlated-k model for the longwave. *J. Geophys. Res.*, **102**, 16 663–16 682, https://doi.org/10.1029/97JD00237.

Moncrieff, M. W., D. E. Waliser, M. J. Miller, M. A. Shapiro, G. R. Asrar, and J. Caughey, 2012: Multiscale convective organization and the YOTC Virtual Global Field Campaign. *Bull. Amer. Meteor. Soc.*, **93**, 1171–1187, https://doi.org/10.1175/BAMS-D-11-00233.1.

Nakazawa, T., 1988: Tropical super clusters within intraseasonal variations over the western Pacific. *J. Meteor. Soc. Japan*, **66**, 823–836, https://doi.org/10.2151/jmsj1965.66.6_823.

Pantillon, F., P. Mascart, J.-P. Chaboureau, C. Lac, J. Escobar, and J. Duron, 2011: Seamless MESO-NH modeling over very large grids. *C. R. Mec.*, **339**, 136–140, https://doi.org/10.1016/j.crme.2010.12.002.

Pauluis, O. M., and A. A. Mrowiec, 2013: Isentropic analysis of convective motions. *J. Atmos. Sci.*, **70**, 3673–3688, https://doi.org/10.1175/JAS-D-12-0205.1.

Pergaud, J., V. Masson, S. Malardel, and F. Couvreux, 2009: A parameterization of dry thermals and shallow cumuli for mesoscale numerical weather prediction. *Bound.-Layer Meteor.*, **132**, 83–106, https://doi.org/10.1007/s10546-009-9388-0.

Pinty, J.-P., and P. Jabouille, 1998: A mixed-phase cloud parameterization for use in a mesoscale non-hydrostatic model: Simulations of a squall line and of orographic precipitations. *Conf. on Cloud Physics*, Everett, WA, Amer. Meteor. Soc., 217–220.

Wang, S., A. H. Sobel, F. Zhang, Y.Q. Sun, Y. Yue, and L. Zhou, 2015: Regional simulation of the October and November MJO events observed during the CINDY/DYNAMO field campaign at gray zone resolution. *J. Climate*, **28**, 2097–2119, https://doi.org/10.1175/JCLI-D-14-00294.1.

Yoneyama, K., C. Zhang, and C. N. Long, 2013: Tracking pulses of the Madden–Julian oscillation. *Bull. Amer. Meteor. Soc.*, **94**, 1871–1891, https://doi.org/10.1175/BAMS-D-12-00157.1.

Zhang, C., 2005: Madden–Julian oscillation. *Rev. Geophys.*, **43**, RG2003, https://doi.org/10.1029/2004RG000158.

——, and K. Yoneyama, 2017: CINDY/DYNAMO field campaign: Advancing our understanding of MJO initiation. *The Global Monsoon System*, C.-P. Chang et al., Eds., World Scientific Series on Asia-Pacific Weather and Climate, Vol. 9, World Scientific Publishing Co., 339–348, https://doi.org/10.1142/9789813200913_0027.

——, J. Gottschalck, E. D. Maloney, M. W. Moncrieff, F. Vitart, D. E. Waliser, B. Wang, and M. C. Wheeler, 2013: Cracking the MJO nut. *Geophys. Res. Lett.*, **40**, 1223–1230, https://doi.org/10.1002/grl.50244.